

Numerical Simulations of Mountain Waves in the Middle Atmosphere over the Southern Andes

Kwok-Aun Tan

School of Mathematics, University of New South Wales, Sydney, Australia

Stephen D. Eckermann

E. O. Hulbert Center for Space Research, Naval Research Laboratory, Washington, DC

We use a two-dimensional nonlinear compressible mesoscale model to study mountain waves in the middle atmosphere over the southern Andes. Using realistic temperatures, winds and topography, the model generates large-amplitude long-wavelength breaking mountain waves in the middle atmosphere that compare favorably with satellite measurements. Modeled waves have preferred horizontal wavelengths. Spectral analysis reveals correspondences between these wavelengths and peaks in the spectrum of Andean topographic elevations. The shorter waves reach the stratosphere well before the longer ones, consistent with group velocity arguments, with longer wavelengths ultimately dominating. At later times we find evidence of downward propagating secondary waves produced by upper-level breaking of the primary waves.

1. INTRODUCTION

Theory and parameterization have indicated that gravity waves forced by flow over mountains are a major source of dynamical driving for the stratosphere and mesosphere [e.g., Bacmeister, 1993; Boville, 1995]. Detailed mesoscale model simulations have proved useful in modeling mountain wave dynamics and refining simpler parameterizations of these processes in the troposphere and lower stratosphere [e.g., Laprise, 1993; Kim and Arakawa, 1995; Durran, 1995; Broad, 1996; Dörnbrack *et al.*, 1998].

However, only a few such models have incorporated a middle atmosphere and investigated mountain wave dynamics up to and beyond the stratopause. One of the first relatively detailed studies was by Schoeberl [1985], who derived

linear nonhydrostatic mountain wave solutions within realistic wind profiles from the ground up to ~ 70 – 80 km. More detailed numerical simulations were performed by Bacmeister and Schoeberl [1989] using a two-dimensional nonlinear time-dependent anelastic model of flow over an obstacle. They found zones of strong wave overturning in the middle atmosphere that generated secondary downward-propagating waves. Their model used idealized representations of the background atmosphere. Satomura and Sato [1999] used a fully nonlinear compressible two-dimensional model of flow over orography with realistic representations of the lower and middle atmospheres, based on climatology. They too simulated strong wave breaking in the middle stratosphere and generation of secondary waves from these unstable regions, although the wavelengths differed from those found by Bacmeister and Schoeberl [1989]. All of these studies considered flow over a bell-shaped obstacle and omitted Coriolis accelerations.

Here, we take further steps towards “real world” mesoscale model simulations of mountain waves in the middle atmosphere. Our simulations focus on a specific set of satellite

Report Documentation Page			<i>Form Approved OMB No. 0704-0188</i>	
<p>Public reporting burden for the collection of information is estimated to average 1 hour per response, including the time for reviewing instructions, searching existing data sources, gathering and maintaining the data needed, and completing and reviewing the collection of information. Send comments regarding this burden estimate or any other aspect of this collection of information, including suggestions for reducing this burden, to Washington Headquarters Services, Directorate for Information Operations and Reports, 1215 Jefferson Davis Highway, Suite 1204, Arlington VA 22202-4302. Respondents should be aware that notwithstanding any other provision of law, no person shall be subject to a penalty for failing to comply with a collection of information if it does not display a currently valid OMB control number.</p>				
1. REPORT DATE 2000	2. REPORT TYPE	3. DATES COVERED 00-00-2000 to 00-00-2000		
4. TITLE AND SUBTITLE Numerical Simulations of Mountain Waves in the Middle Atmosphere over the Southern Andes			5a. CONTRACT NUMBER	
			5b. GRANT NUMBER	
			5c. PROGRAM ELEMENT NUMBER	
6. AUTHOR(S)			5d. PROJECT NUMBER	
			5e. TASK NUMBER	
			5f. WORK UNIT NUMBER	
7. PERFORMING ORGANIZATION NAME(S) AND ADDRESS(ES) Naval Research Laboratory, E.O. Hulburt Center for Space Research, Washington, DC, 20375			8. PERFORMING ORGANIZATION REPORT NUMBER	
9. SPONSORING/MONITORING AGENCY NAME(S) AND ADDRESS(ES)			10. SPONSOR/MONITOR'S ACRONYM(S)	
			11. SPONSOR/MONITOR'S REPORT NUMBER(S)	
12. DISTRIBUTION/AVAILABILITY STATEMENT Approved for public release; distribution unlimited				
13. SUPPLEMENTARY NOTES				
14. ABSTRACT				
15. SUBJECT TERMS				
16. SECURITY CLASSIFICATION OF:			17. LIMITATION OF ABSTRACT Same as Report (SAR)	18. NUMBER OF PAGES 8
a. REPORT unclassified	b. ABSTRACT unclassified	c. THIS PAGE unclassified	19a. NAME OF RESPONSIBLE PERSON	

measurements of mountain waves over the region shown in Plate 1a. Colored squares, labeled 1,2 and 3, show locations of three successive vertical temperature profiles acquired by the Cryogenic Infrared Spectrometers and Telescopes for the Atmosphere (CRISTA) on 6 November, 1994 at 6:24 UT. These profiles, reproduced in Plate 4 of Grossman [2000], reveal coherent stratospheric temperature oscillations. Eckermann and Preusse [1999] used theory and parameterization to argue that these oscillations were large-scale mountain waves generated by flow over the Andes.

In section 2, we show that two-dimensional mesoscale model simulations offer a potentially useful means of studying the generation and evolution of the mountain waves observed on this day. We describe our mesoscale model in section 3, and apply it in section 4 using “best” estimates of the large-scale winds, temperatures and orography. The results are analyzed in section 5 and the findings are summarized in section 6.

2. CRISTA OBSERVATIONS AND REGIONAL DOMAIN

Plate 1 shows that the large-scale topography here is quasi-two dimensional. The “ridge axis” in Plate 1a is a subjective fit to the orientation of the long axis of the Andes. The “perpendicular axis,” aligned normal to this ridge axis, passes as close as possible to the three CRISTA profiles, and illustrates that the CRISTA data were acquired along an orbital segment that passed nearly orthogonally across the ridge axis of the Andes.

We take the blue dot in Plate 1 at the western end of the perpendicular axis as our “upstream point,” since surface winds were eastward and the atmosphere here is far enough upstream to remain unaffected by the Andes [Seluchi *et al.*, 1998]. Figure 1a plots a hodograph of the horizontal wind profile at the upstream point on 6 November, 1994 at 6:00 UT, using data from NASA’s Data Assimilation Office [Coy and Swinbank, 1997]. Upstream troposphere-stratosphere winds were roughly parallel to the perpendicular axis at this time, particularly near the surface and in the stratosphere, our primary regions of interest. Maximum deviations of $\sim 45^\circ$ occurred near the tropopause in Figure 1a.

Similar conditions occur when eastward surface winds flow in from the ocean across the Norwegian Mountains. In these situations, three-dimensional mesoscale models often predict long two-dimensional (plane) mountain waves in the lower stratosphere over Scandinavia, which compare well with aircraft and radiosonde data [Leutbecher and Volkert, 1996; Dörnbrack *et al.*, 1998, 1999]. Consequently, these waves can be modeled fairly accurately using a two-dimensional mesoscale model [Volkert and Intes, 1992]. We too use a two-dimensional mesoscale model as a first step in this study.

3. NUMERICAL MODEL AND DOMAIN

3.1. Model Description

The model used here was developed from an earlier version first described by Tan and Leslie [1998]. It solves the Euler equations for fully compressible nonlinear nonhydrostatic atmospheric flow over arbitrary terrain in a two-dimensional spatial domain. The velocity $\mathbf{u} = (u, v, w)$, potential temperature θ and Exner pressure π are split into background and perturbation terms, as follows:

$$\begin{aligned} u(x, z, t) &= \bar{u}(z) + u'(x, z, t), \\ \theta(x, z, t) &= \bar{\theta}(z) + \theta'(x, z, t), \\ \pi(x, z, t) &= \bar{\pi}(z) + \pi'(x, z, t). \end{aligned}$$

The velocity components v and w contain perturbation terms only. A background temperature profile $\bar{T}(z)$ is used to initialize the background density $\bar{\rho}(z)$, potential temperature $\bar{\theta}(z)$ and Exner pressure $\bar{\pi}(z) = \bar{T}(z)/\bar{\theta}(z)$, assuming hydrostatic equilibrium. The cross-ridge background flow, $\bar{u}(z)$, is assumed to be in thermal wind balance. The momentum, thermodynamic and continuity equations become:

$$\frac{du'}{dt} + w' \frac{\partial \bar{u}}{\partial z} + c_p \theta \frac{\partial \pi'}{\partial x} - fv' = D(u'), \quad (1a)$$

$$\frac{dv'}{dt} + fu' = D(v'), \quad (1b)$$

$$\frac{dw'}{dt} + c_p \theta \frac{\partial \pi'}{\partial z} - g \frac{\theta'}{\bar{\theta}} = D(w'), \quad (1c)$$

$$\frac{d\theta'}{dt} + w' \frac{\partial \bar{\theta}}{\partial z} = D(\theta'), \quad (1d)$$

$$\frac{d\pi'}{dt} + w' \frac{\partial \bar{\pi}}{\partial z} + \frac{c_s^2}{c_p \bar{\rho} \bar{\theta}^2} \nabla \cdot (\bar{\rho} \bar{\theta} \mathbf{u}') = 0, \quad (1e)$$

where

$$\begin{aligned} \nabla \cdot (\bar{\rho} \bar{\theta} \mathbf{u}') &\equiv \left(\frac{\partial(\bar{\rho} \bar{\theta} u')}{\partial x} + \frac{\partial(\bar{\rho} \bar{\theta} w')}{\partial z} \right), \\ \frac{d}{dt} &\equiv \frac{\partial}{\partial t} + (\bar{u} + u') \frac{\partial}{\partial x} + w' \frac{\partial}{\partial z}, \end{aligned}$$

c_p and c_v are the mass specific heats at constant pressure and volume, respectively, $R = c_p - c_v$ is the gas constant for dry air, g is the gravitational acceleration, c_s is the speed of sound and f is the Coriolis parameter. The $D(X')$ terms in (1a)–(1d) are damping terms for the perturbation quantities X' , and represent the combined effects of a first-order turbulence closure scheme [Lilly, 1962], fourth-order computational damping (to suppress small-scale numerical modes),

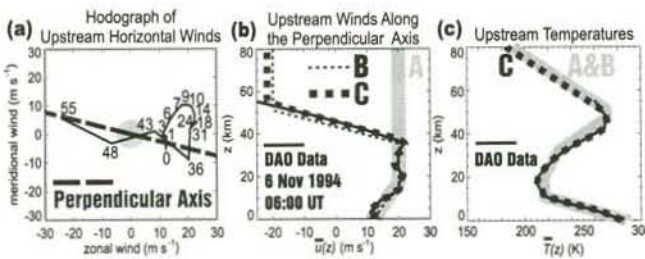


Figure 1. (a) Hodograph of horizontal winds over the upstream point in Figure 1, taken from DAO assimilated data on 6 November, 1994, 6:00 UT. The altitudes (in kilometers) of each wind value are labeled along the hodograph trace. Orientation of the perpendicular axis in Plate 1a is shown with a broken line; (b) black solid curve shows the upstream DAO winds along the perpendicular axis, $\bar{u}(z)$. Other labeled curves show model $\bar{u}(z)$ profiles used in Experiments A, B and C; (c) vertical profile of upstream DAO temperatures (solid black curve), and the model curves used in Experiments A, B and C.

and a sponge layer (Rayleigh damping) at upper levels [Durran and Klemp, 1983].

To incorporate topography at the bottom boundary, the model uses the terrain-following vertical coordinate

$$\zeta(x, z) = \frac{L[z - h(x)]}{L - h(x)}, \quad (2)$$

where L is the top model altitude and $h(x)$ is the topographic height function [Gal-Chen and Sommerville, 1975]. A free-slip lower boundary condition is used.

The model equations (1a)–(1e) are solved numerically using the Klemp-Wilhelmson time-splitting method on an Arakawa C-grid [Klemp and Wilhelmson, 1978; Durran and Klemp, 1983; Wicker and Skamarock, 1998]. The second-order Runge-Kutta method is used for the large time steps, Δt_l , and the forward-backward scheme is used for the small time steps, Δt_s . An implicit method is used in the vertical for the acoustic terms in the governing equations. A third-order upwind finite difference scheme is used for the advection terms and second-order centered finite differencing is used for the pressure gradient and divergence terms. The Miller-Thorpe radiation condition is used at the lateral boundaries to prevent side reflections [Miller and Thorpe, 1981]. The current model configuration was validated by reproducing mountain wave patterns from previous two-dimensional model experiments [e.g., Doyle *et al.*, 2000].

3.2. Model Domain and Initialization

The perpendicular axis x in Plate 1 extended to 3000 km in our model with a grid resolution $\Delta x = 2$ km. We set the model lid $L = 80$ km and vertical resolution $\Delta z = 0.5$ km. Topographic elevations $h(x)$ in Plate 1b were smoothed to remove the two and four grid-point wavelengths that can

cause numerical aliasing. In all experiments, wind profiles were ramped up over 2 hours from an initial state of rest, to minimize the generation of transient oscillations [e.g., Ikawa, 1990]. The upper-level sponge was effective above ~ 55 km. Equations were forwarded using $\Delta t_l = 5$ s and $\Delta t_s = 1$ s.

4. MODEL SIMULATIONS

4.1. Experiments A, B and C

Three different model experiments, denoted A, B and C, were conducted. As shown in Figures 1b and 1c, each successive experiment more closely approximated the upstream DAO wind and temperature profiles at the time of the CRISTA measurements.

Experiment A used an idealized wind profile $\bar{u}(z)$ that omitted the westward shear layer in the DAO profile above 35 km (Figure 1b). This control experiment allowed us to study mountain wave generation and propagation without the complication of critical-level effects ($\bar{u}(z) = 0$).

In Experiment B, a linear westward shear layer was introduced above 35 km, yielding $\bar{u}(z) = 0$ at $z \approx 43$ km. Experiment B allowed us to introduce the critical layer, while maintaining an identical atmospheric situation to Experiment A below 35 km. To this end, both experiments used background temperatures $\bar{T}(z)$ from the 1976 U.S. Standard Atmosphere at mid-latitudes [Minzner, 1977], which fit the upstream DAO temperatures from ~ 0 –55 km quite well (Figure 1c).

Experiment C used cubic spline fits to the DAO wind and temperature profiles from 0–55 km. This yielded a zero wind line at $z \approx 46$ km, slightly higher than in Experiment B. Lacking DAO data above 55 km, from 55–80 km we used constant winds and a linear temperature gradient equal to that in Experiments A and B.

4.2. Results

In all three experiments, mountain waves entered the middle atmosphere after a few hours and produced overturning isentropes after ~ 6 hours. We focus on temperatures since CRISTA measured temperature perturbations. Plate 2 plots potential temperatures $\theta(x, \zeta, t)$ and temperature perturbations $T'(x, \zeta, t)$ after $t = 18$ hours over the orographic region in each experiment. The critical levels in Experiments B and C efficiently absorb mountain waves, and yield rapid wave shortening and intense breaking at closely underlying altitudes. Despite the different wind profiles and the significant amounts of overturning and mixing by this time, the large-scale wave structures below 35 km are quite similar in each experiment.

The wave fields evolve significantly with time, as illustrated in Figure 2 using results from Experiment C. The middle atmosphere is dominated initially by short horizontal wavelengths, which trigger vigorous overturning and mixing by 8 hours. The turbulent zones persist and seem to move

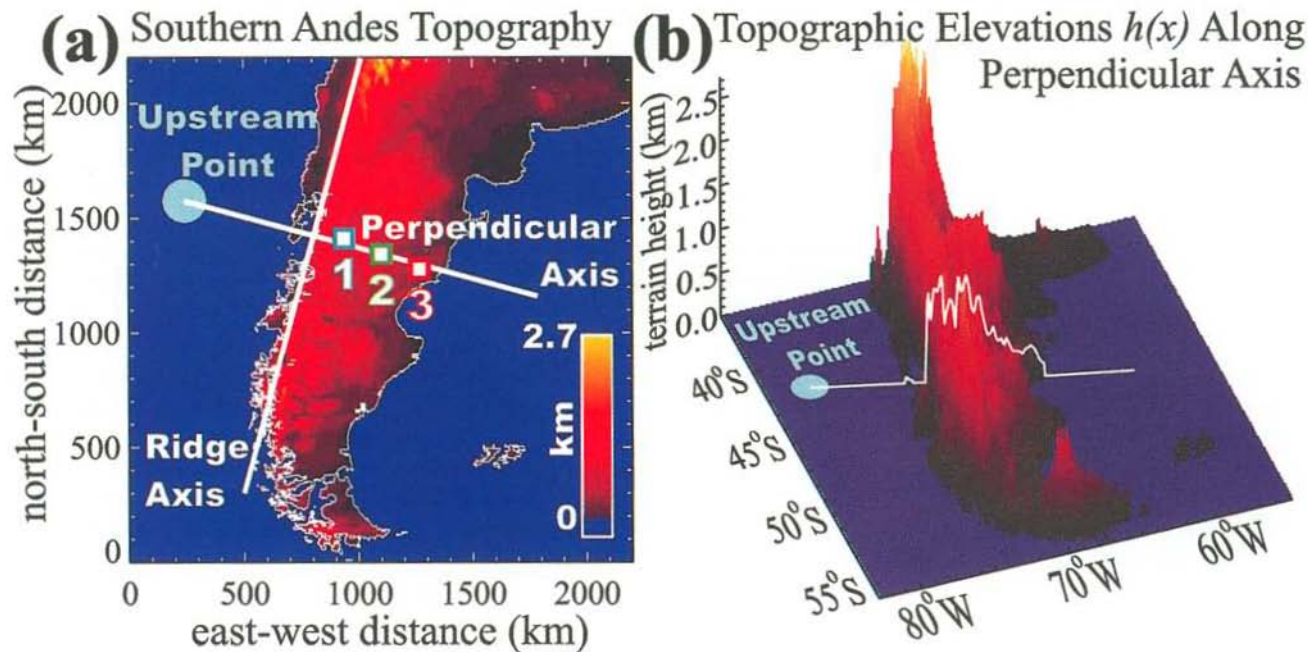


Plate 1. Topographic elevations over southern South America, plotted as (a) filled contours in Cartesian coordinates, (b) three-dimensional elevations in Mercator coordinates. Squares labeled 1,2 and 3 in (a) show locations of temperature profiles acquired by CRISTA. Raw elevations $h(x)$ along the perpendicular axis in (a) are plotted in (b). The blue dot in both figures is the upstream point. See text for further details.

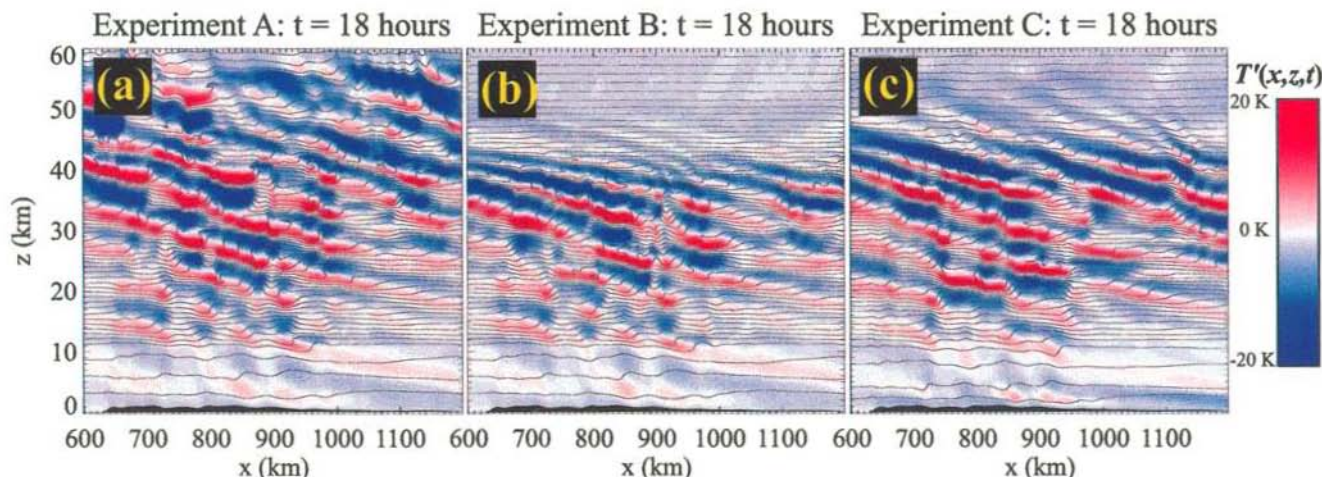


Plate 2. Temperature fields after 18 hours in Experiments A, B and C. Contours show isentropes $\theta(x, \zeta, t)$, with constant logarithmic separation between adjacent contours. Temperature perturbations $T'(x, \zeta, t)$ are overlaid using the blue-red color scheme shown to the right. Underlying topography is shown in black.

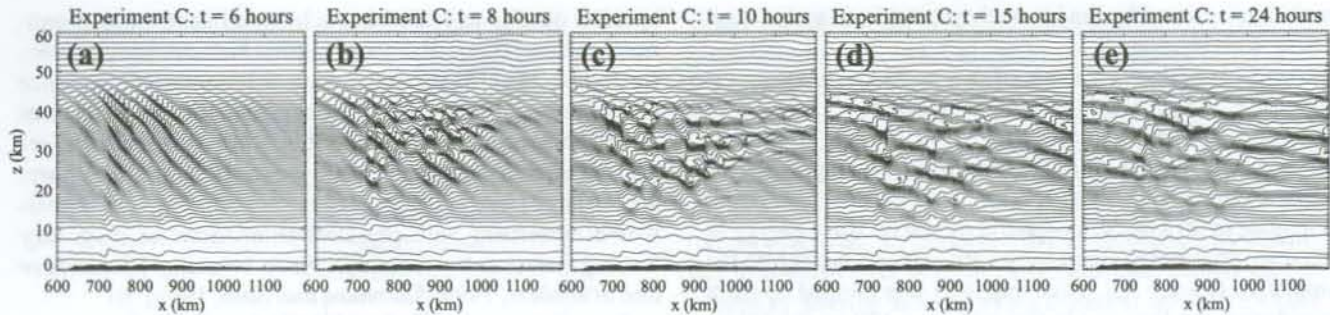


Figure 2. Isentropes $\theta(x, \zeta, t)$ from Experiment C after $t = 6, 8, 10, 15$ and 24 hours. Same constant logarithmic separation between contours is used in each panel. Underlying topography is shaded.

downstream after 10 hours. Thereafter, progressively longer horizontal wavelengths come to dominate the wave field, and less vigorous overturning is evident. After 24 hours, waves at lower stratospheric levels are suppressed compared to their earlier intensities.

5. ANALYSIS

5.1. Wavelength Selection

Preferred vertical wavelengths are evident in Plate 2 and Figure 2. The vertical wavelength of a stationary hydrostatic mountain wave is given theoretically by

$$\lambda_z(z) \approx \frac{2\pi\bar{u}(z)}{N(z)}, \quad (3)$$

where N is Brunt-Väisälä frequency and π has its usual meaning here. At 15–30 km, $\bar{u}(z) = 20 \text{ m s}^{-1}$ and $N = 0.021 \text{ rad s}^{-1}$, which yields $\lambda_z = 6 \text{ km}$, in agreement with the dominant vertical wavelengths found below 35 km in all three experiments. In Experiments B and C, where westward shear was introduced above 35 km, λ_z decreases with height in accordance with (3).

Preferred horizontal wavelengths λ_x also emerged in each experiment (Figure 2). We studied this spectrally by regridding $T'(x, \zeta, t)$ fields onto a regular height grid z , then computing two-dimensional power spectra $F_T(K, M)$ over the range $x = 250$ –1250 km and $z = 12$ –32 km. As expected from (3), for all K a sharp spectral peak occurred at a vertical wavenumber $|\tilde{M}| \approx 2\pi(6 \text{ km})^{-1}$, enabling us to study overall spectral variability in these simulations using the one-dimensional spectral slice $F_T(K, M \approx \tilde{M})$.

Spectra from each experiment are plotted in Figure 3 after 6, 15 and 24 hours. The power spectrum of the topography $h(x)$ is plotted in Figure 3d, with evident peaks marked by light solid lines. These same lines are also plotted in the other panels of Figure 3, and show that peaks in stratospheric temperature spectra correspond quite well with peaks in the topographic spectrum. Thus, horizontal wavelength selection seems to be governed by spectral features in the Andean topography.

5.2. Time Evolution

Figures 2 and 3 show that the dominant horizontal wavelengths change with time. Short λ_x values dominate the middle atmosphere initially, giving way to progressively longer horizontal wavelengths at later times. The vertical group velocity of any hydrostatic wave ($\lambda_z^2/\lambda_x^2 \ll 1$) is given by

$$c_{gz} = \frac{\partial \omega}{\partial m} = \frac{\lambda_z^2 N(z)}{2\pi\lambda_x}. \quad (4)$$

From (3), all waves below 35 km have similar vertical wavelengths λ_z , and so the vertical group velocities of various

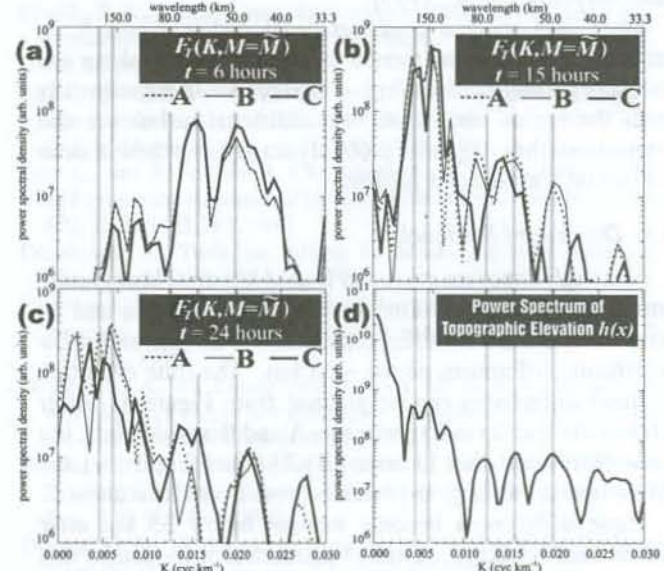


Figure 3. One-dimensional sections of the two-dimensional power spectra $F_T(K, M)$ at $M = \tilde{M} = 1/6 \text{ cyc km}^{-1}$ from Experiments A, B and C after (a) 6 hours, (b) 15 hours, and (c) 24 hours. Spectra were computed from $T'(x, z, t)$ fields in the region $z = 12$ –32 km and $x = 250$ –1250 km. Since \tilde{M} straddles the third and fourth harmonics of these spectra, we plot averages of the slices at these two harmonics. Panel (d) plots power spectral density of the topographic elevation $h(x)$. Local maxima in (d) are highlighted with gray vertical lines, and are also shown in the preceding panels.

mountain wave modes are inversely proportional to their horizontal wavelengths, λ_x .

Using (3) and (4), a wave of $\lambda_x = 50$ km has a group velocity $c_{gz} \approx 2.5 \text{ m s}^{-1}$, and thus takes ~ 3.5 hours to propagate to $z = 30$ km. Spectra in Figure 3a confirm that the peak near $\lambda_x = 50$ km is fully developed after 6 hours. Conversely, a $\lambda_x = 150$ km wave takes ~ 10 hours to propagate to 30 km. Stratospheric mountain wave energy at this scale does not develop fully until ~ 10 –15 hours into the simulation (Figure 3b). Note that $\bar{u}(z)$ was ramped up from zero during the first two hours, and was $< 20 \text{ m s}^{-1}$ below 17 km, making actual propagation times somewhat longer.

The mean width of the topography $h(x)$ is ~ 300 –500 km (see Plate 1), which might be expected to force a $\lambda_x \sim 300$ –500 km wave most strongly. Indeed, ridge widths here are similar to those in northern Scandinavia, where very long mountain waves often dominate the stratospheric wave field [Dörnbrack *et al.*, 1998, 1999]. Using (3) and (4), after 24 hours a 400 km wave would have propagated to a height of only 20 km or so, and thus would not be fully developed in the middle atmosphere. Spectra after 24 hours confirm this: while Experiments A and B show a peak at a wavelength ~ 400 –500 km in Figure 3c, spectra from Experiment C peak most strongly nearer 200–250 km. Thus, longer simulations are needed to assess whether a $\lambda_x \sim 400$ km wave eventually dominates the middle atmospheric wave fluctuations [see also Dörnbrack *et al.*, 1999].

Once each spectral peak has developed in Figure 3, its intensity tends to wane thereafter, due to wave breaking and increasing turbulent damping. As longer waves subsequently enter the region and break, the additional turbulence and interactions they engender probably act to damp these shorter horizontal wavelengths further.

5.3. Downward Feedback

Although Experiments A and B used identical background atmospheres below 35 km, the results in Plates 2a and 2b after 18 hours are identical only below ~ 20 km, and show significant differences above ~ 25 km. The time evolution of these differences can be gleaned from Figure 3. After 6 hours the spectra in Experiments A and B are identical, but show differences after 15 hours. By 24 hours (Figure 3c), the differences are as large in places as those from Experiment C.

These differences become evident below 35 km after waves start breaking. Implicit numerical diffusion in this model is very small, so these differences must originate from downward feedback of differing dynamics originating above 35 km, where different $\bar{u}(z)$ profiles yield different wave and turbulence fields. Turbulence itself cannot be advected this far downwards, since we include no mean vertical wind.

Two-dimensional spectra $F_T(K, M)$ separate upward and downward propagating waves [e.g., Bacmeister and Schoeberl, 1989]: only the upward components are plotted in Figure 3. After 12–24 hours, significant downward-propagating

spectral density appeared in each experiment, most prominently at long horizontal wavelengths. Vertical velocity spectra $F_T(K, M)$ also showed downward propagating variance at shorter horizontal scales. The appearance of these features in Experiment A indicates that this is not a critical-level reflection effect, as expected since mean Richardson numbers are too large [Jones, 1968]. Rather, these findings are in qualitative agreement with previous simulations of secondary wave generation by mountain wave breaking [Bacmeister and Schoeberl, 1989; Satomura and Sato, 1999].

Bacmeister and Schoeberl [1989] found that their downward propagating secondary waves eventually led to reductions in overall wave intensity well below the regions of wave breaking. Attenuated wave activity at lower levels also arose in our simulations (Figure 2e). Whether the attenuation noted here results mostly from the effects of downward propagating secondary waves, or from breakdown of and additional turbulent damping by progressively longer upward-propagating primary waves, is unclear at present.

5.4. Comparison with CRISTA Profiles

The general form of the profiles over the Andes compares favorably with the CRISTA data. Figure 4 plots a sample temperature perturbation profile from Experiment C at $x = 845$ km, a location between points 1 and 3 in Plate 1a. The CRISTA profiles at these points are overlayed [see Plate 4 of Grossmann, 2000]. The wavelength, amplitude and general height variation of the model profile are all quite similar to the data. Oscillations in Experiment C seem to penetrate slightly higher prior to shortening and dissipating below the critical layer. Note too that the amplitudes of the CRISTA profiles are probably underestimated due to instrumental effects, and that CRISTA cannot resolve any waves of $\lambda_z \lesssim 3$ –5 km [Eckermann and Preusse, 1999].

Model profiles from locations directly over points 1 and 3 are not in phase with the CRISTA perturbations. This is due to somewhat different horizontal wavelengths in the model simulations. Eckermann and Preusse [1999] showed that the oscillations measured by CRISTA had a horizontal wavelength of either 400 km or $400/3 \approx 130$ km. Peaks somewhat near these values appear in Figure 3c, although other peaks also occur and there are variations among the experiments.

6. SUMMARY AND DISCUSSION

We have developed a high-resolution high-altitude nonlinear numerical model of compressible atmospheric flow over arbitrary topography, and have used it here to simulate mountain waves in the middle atmosphere over the southern Andes. The results have confirmed that stratospheric temperature perturbations measured by CRISTA on 6 November, 1994 were produced by intense breaking mountain waves forced by flow over the southern Andes, as argued by Eckermann

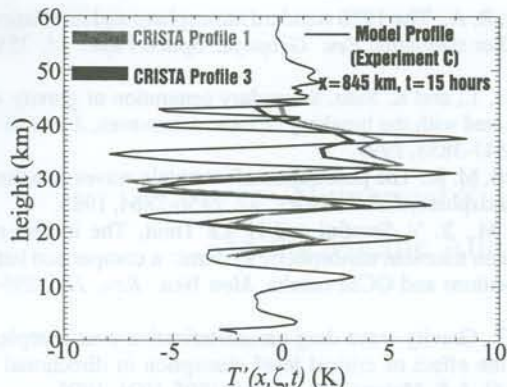


Figure 4. Black curve shows a vertical profile of temperature perturbations at $x = 845$ km, 15 hours into Experiment C. Two shaded solid curves reproduce the temperature perturbation profiles acquired by CRISTA at locations 1 and 3 in Plate 1a (after Eckermann and Preusse [1999]).

and Preusse [1999]. Amplitudes and vertical wavelengths from CRISTA compare fairly well with model profiles. The results showed that attenuated oscillations above 30 km were the result of vertical wavelength reductions and intense wave breaking, as conjectured by Eckermann and Preusse [1999]. Recent analysis of satellite data by McLandress *et al.* [2000] has shown that temperature fluctuations appear recurrently in the middle atmosphere over southern South America. Thus these breaking mountain waves may be relevant to the climatology of this region of the middle atmosphere [Garcia and Boville, 1994].

Presently we have a limited understanding of the amplitudes and wavelengths of mountain waves radiated into the middle atmosphere by complex topography. Existing parameterizations make use of topographic elevation spectra, focusing either on dominant peaks [e.g., Bacmeister, 1993] or their power-law shapes [e.g., Shutts, 1995] to specify radiated mountain wave fields. Our results, though limited to a specific two-dimensional section of the Andes, produced stratospheric wave fluctuations with distinct vertical and horizontal wavelengths. These horizontal wavelengths were closely related to peaks in the power spectrum of the topographic elevations $h(x)$, lending some support to spectral parameterization methods. However, the various horizontal wavelengths evolved differently with time in our model, due mostly to varying vertical group velocities. Wave fields were further complicated at later times by breaking and turbulence, leading not only to increased damping of primary waves but apparent generation of secondary waves. Even after 24 hours, when simulations were terminated due to computational constraints, mountain waves in the middle atmosphere were still evolving.

Actual topography and flow fields here are intrinsically three-dimensional [Plate 1b; Figure 1a; Seluchi *et al.*, 1998], which can influence mountain waves significantly [Shutts,

1998]. While two-dimensional models with turbulence parameterizations provide reasonable simulations of breaking gravity waves [Liu *et al.*, 1999; Doyle *et al.*, 2000], long-term fine-scale simulations of wave breakdown beneath a critical level seem to require three-dimensional models [Winters and D'Asaro, 1994; Dörnbrack, 1998; Fritts and Werne, 2000]. Additionally, the model here did not include mean flow evolution, which may be important in this problem. Thus, multi-day interactive runs using three-dimensional models may be needed to describe these evolving mountain wave fields fully.

Acknowledgments. These simulations were made possible by a grant of computing time on the Australian National University Supercomputing Facility's Fujitsu VPP300 vector supercomputer. SDE acknowledges support for this research by the Office of Naval Research and by NASA through the Atmospheric Chemistry Modeling and Analysis Program and the UARS Guest Investigator Program. We thank D. Broutman, A. Dörnbrack, P. Preusse and two reviewers for helpful comments on earlier drafts.

REFERENCES

- Bacmeister, J. T., Mountain-wave drag in the stratosphere and mesosphere inferred from observed winds and a simple mountain-wave parameterization scheme, *J. Atmos. Sci.*, 50, 377-399, 1993.
- Bacmeister, J. T., and M. R. Schoeberl, Breakdown of vertically propagating two-dimensional gravity waves forced by orography, *J. Atmos. Sci.*, 46, 2109-2134, 1989.
- Boville, B. A., Middle atmosphere version of the CCM2 (MACCM2): annual cycle and interannual variability, *J. Geophys. Res.*, 100, 9017-9039, 1995.
- Broad, A. S., High resolution numerical-model integrations to validate gravity-wave-drag parameterization schemes: a case study, *Q. J. R. Meteorol. Soc.*, 122, 1625-1653, 1996.
- Coy, L., and R. Swinbank, Characteristics of stratospheric winds and temperatures produced by data assimilation, *J. Geophys. Res.*, 102, 25,763-25,781, 1997.
- Dörnbrack, A., Turbulent mixing by breaking gravity waves, *J. Fluid Mech.*, 375, 113-141, 1998.
- Dörnbrack, A., M. Leutbecher, H. Volkert and M. Wirth, Mesoscale forecasts of stratospheric mountain waves, *Meteorol. Appl.*, 5, 117-126, 1998.
- Dörnbrack, A., M. Leutbecher, R. Kivi and E. Kyrö, Mountain-wave-induced record low stratospheric temperatures above northern Scandinavia, *Tellus*, 51A, 951-963, 1999.
- Doyle, J. D., et al., An intercomparison of model-predicted wave breaking for the 11 January 1972 Boulder windstorm, *Mon. Wea. Rev.*, 128, 901-914, 2000.
- Durran, D. R., Do breaking mountain waves decelerate the local mean flow?, *J. Atmos. Sci.*, 52, 4010-4032, 1995.
- Durran, D. R., and J. B. Klemp, A compressible model for the simulation of moist mountain waves, *Mon. Wea. Rev.*, 111, 2341-2361, 1983.
- Eckermann, S. D., and P. Preusse, Global measurements of stratospheric mountain waves from space, *Science*, 286, 1534-1537, 1999.
- Fritts, D. C., and J. A. Werne, Turbulence dynamics and mixing due to gravity waves in the lower and middle atmosphere, *this volume*.
- Gal-Chen, T., and R. C. T. Sommerville, On the use of a coordinate

transformation for the solution of the Navier-Stokes equations, *J. Comp. Phys.*, 17, 209-228, 1975.

Garcia, R. R., and B. A. Boville, "Downward control" of the mean meridional circulation and temperature distribution of the polar winter stratosphere, *J. Atmos. Sci.*, 51, 2238-2245, 1994.

Grossmann, K. U., Recent improvements in middle atmosphere remote sounding techniques: the CRISTA-SPAS experiment, *this volume*.

Ikawa, M., High-drag states and foehns of a two-layered stratified fluid past a two-dimensional obstacle, *J. Meteorol. Soc. Japan.*, 68, 163-182, 1990.

Jones, W. L., Reflexion and stability of waves in stably stratified fluids with shear flow: a numerical study, *J. Fluid Mech.*, 34, 609-624, 1968.

Kim, Y.-J., and A. Arakawa, Improvement of orographic gravity wave parameterization using a mesoscale gravity wave model, *J. Atmos. Sci.*, 52, 1875-1902, 1995.

Klemp, J. B., and R. B. Wilhelmson, The simulation of three-dimensional convective storm dynamics, *J. Atmos. Sci.*, 35, 1070-1096, 1978.

Laprise, J. P. R., An assessment of the WKBJ approximation to the vertical structure of linear mountain waves: implications for gravity wave drag parameterization, *J. Atmos. Sci.*, 50, 1469-1487, 1993.

Leutbecher, M., and H. Volkert, Stratospheric temperature anomalies and mountain waves: A three-dimensional simulation using a multi-scale weather prediction model, *Geophys. Res. Lett.*, 23, 3329-3332, 1996.

Lilly, D. K., On the numerical simulation of buoyant convection, *Tellus*, 14, 148-172, 1962.

Liu, H.-L., P. B. Hays, and R. G. Roble, A numerical study of gravity wave breaking and impacts on turbulence and mean state, *J. Atmos. Sci.*, 56, 2152-2177, 1999.

McLandress, C., M. J. Alexander, and D. L. Wu, Microwave Limb Sounder observations of gravity waves in the stratosphere: a climatology and interpretation, *J. Geophys. Res.*, (in press), 2000.

Miller, M. J. and A. J. Thorpe, Radiation conditions for the lateral boundaries of limited-area numerical models, *Q. J. R. Meteorol. Soc.*, 107, 615-628, 1981.

Minzner, R. A., The 1976 standard atmosphere and its relationship to earlier standards, *Rev. Geophys. Space Phys.*, 15, 255-264, 1977.

Satomura, T., and K. Sato, Secondary generation of gravity waves associated with the breaking of mountain waves, *J. Atmos. Sci.*, 56, 3847-3858, 1999.

Schoeberl, M. R., The penetration of mountain waves into the middle atmosphere, *J. Atmos. Sci.*, 42, 2856-2864, 1985.

Seluchi, M., Y. V. Serafini and H. Le Treut, The impact of the Andes on transient atmospheric systems: a comparison between observations and GCM results, *Mon Wea. Rev.*, 126, 895-912, 1998.

Shutts, G., Gravity-wave drag parameterization over complex terrain: the effect of critical level absorption in directional wind shear, *Q. J. R. Meteorol. Soc.*, 121, 1005-1021, 1995.

Shutts, G. J., Stationary gravity-wave structure in flows with directional wind shear, *Q. J. R. Meteorol. Soc.*, 124, 1421-1442, 1998.

Tan, K. A., and L. M. Leslie, Development of a non-hydrostatic model for atmospheric modelling, in *Computational Techniques and Applications: CTAC97*, edited by B.J. Noye, M.D. Teubner, and A.W. Gill, pp. 679-686, World Scientific Press, Singapore, 1998.

Volkert, H., and D. Intes, Orographically forced stratospheric waves over northern Scandinavia, *Geophys. Res. Lett.*, 19, 1205-1208, 1992.

Wicker, L. J., and W. C. Skamarock, A time-splitting scheme for the elastic equations incorporating second-order Runge-Kutta time differencing, *Mon. Wea. Rev.*, 126, 1992-1999, 1998.

Winters, K. B., and E. A. D'Asaro, Three-dimensional wave instability near a critical level, *J. Fluid Mech.*, 272, 255-284, 1994.

K. Tan, School of Mathematics, University of New South Wales, Sydney, NSW 2052, Australia. (e-mail: K.Tan@unsw.edu.au)

S. D. Eckermann, E. O. Hulbert Center for Space Research, Code 7641.2, Naval Research Laboratory, Washington, DC 20375. (e-mail: eckerman@map.nrl.navy.mil)